OPEN ACCESS
IOP Publishing
Superconductor Science and Technology
Supercond. Sci. Technol. **38** (2025) 035008 (13pp)
https://doi.org/10.1088/1361-6668/ada9d3

Design of NI HTS solenoid for PSI positron production experiment

Jaap Kosse*, Henrique Rodrigues, Michał Duda, Thomas Michlmayr, Stephan Müller, Dmitry Sotnikov, André Brem, Stéphane Sanfilippo and Bernhard Auchmann

Paul Scherrer Institute (PSI), Villigen 5232, Switzerland

E-mail: jaap.kosse@psi.ch

Received 2 October 2024, revised 23 December 2024
Accepted for publication 13 January 2025
Published 11 February 2025

Abstract

This paper presents the design of a non-insulated (NI) high-temperature superconductor (HTS) 15 T solenoid with a 72 mm diameter warm bore, intended for use in the Paul Scherrer Institute positron production (P^3) experiment. The P^3 experiment, scheduled to start in Q3 2026, aims to demonstrate a high-yield positron source that is relevant in the context of FCC-ee. The coils will be solder-impregnated using techniques developed with a small-bore HTS NI coil stack. This magnet produced a magnetic field of 18 T at 12 K and 2 kA, in a cryogen-free, conduction-cooled setup. Similarly, the P^3 magnet will be conduction-cooled by two cryocoolers. This larger-bore magnet is designed to operate at 15 K with a nominal operating current of 1.2 kA. To ensure the protection of the NI magnet, quench prevention is the preferred strategy. Several potential failure modes are analyzed, including thermal runaway in the event of failures in the current leads, power supply, or cryocoolers. By enhancing the cold mass' heat capacity through the addition of a large lead mass, the stored magnetic energy can be safely dissipated in the cold mass through the electrical path formed by the superconductor and the solder. Mechanical analysis indicates that the hoop, radial and axial stresses are kept below allowable limits.

Keywords: non-insulated magnet, HTS magnet, capture solenoid, conduction-cooled, cryogen-free, thermal battery, soldered

1. Introduction

The Paul Scherrer Institute (PSI) positron production (P^3) experiment, scheduled to begin in Q3 2026, aims to demonstrate a high-yield positron source, relevant for future electron–positron collider, in particular a potential future circular collider (FCC-ee) [1, 2]. This document outlines the design of a 15 T non-insulated (NI) high-temperature superconductor (HTS) solenoid with a 72 mm diameter warm bore. The magnet system will be manufactured at the PSI and will constitute a significant component of the experimental hardware for P^3.

The solenoid's function is to capture particles generated by directing an electron beam from the SwissFEL facility at a target located inside the HTS solenoid (figure 1). The target is positioned slightly downstream (3 cm) of the axial center of the solenoid (figure 1), where the axial magnetic field reaches 12.7 T [2]. The downstream fringe field is responsible for the particle bundling [3, 4]. State-of-the-art magnets used for this role are pulsed normal-conducting (NC) magnets, such as those used in SuperKEKB [5], and are known as *flux concentrators* or *adiabatic matching devices*. The advantage of a high yield, defined as the number of captured positrons relative

* Author to whom any correspondence should be addressed.

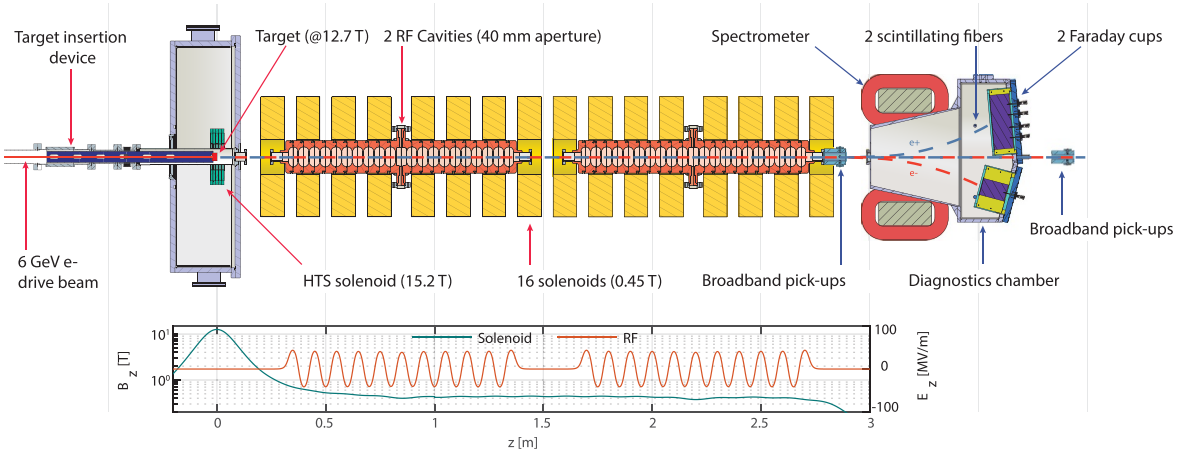

Figure 1. Schematic of the P^3 experiment, adapted from [2]. In this setup, 6 GeV electrons from the FEL, arriving from the left side of the image, are shot at a target located within the bore of the HTS solenoid. This interaction creates a particle shower, which is bundled by the solenoid's stray field. The resulting particle mixture is then accelerated using RF cavities towards a diagnostics module. Normal-conducting solenoids are used to prevent the de-focusing of the particles during the acceleration.

to the number of electrons directed at the target, is the potential reduction in the required target beam intensity for a given number of produced positrons. This, in turn, simplifies the target design, possibly allowing for a stationary target instead of a rotating one [6]. It is estimated that the yield can be increased from approximately 0.6 in state-of-the-art sources [5] to a yield of 7 [3]. However, achieving this high yield relies on using 1.5 T superconducting solenoids around the downstream RF structures. Due to limited resources for this project, 0.45 T NC solenoids will be used for P^3, resulting in an expected yield of 4. Yield is defined as the number of obtained positrons relative to the number of electrons shot at the target.

NI HTS technology gained considerable interest over the last decade, as NI magnets have demonstrated the ability to operate in compact, high current density configurations with high stability [7–9]. For the P^3 experiment, the NI coils are solder-impregnated, resulting in a mechanically strong winding pack. The thermal conductivity provided by the solder, combined with an operating temperature of 15 K, where the available cooling power is large, facilitates conduction-cooled, cryogen-free operation.

In this way, the relatively high deposited power density in the cold mass due to radiation (0.5 mW m^{-3} for FCC-ee [10]) can be effectively removed. The NI paradigm also removes the risk of radiation-induced insulation damage [11]. A major drawback of using NI coils is their long charging time. However, this is not a prohibitive issue for the target solenoid, as it operates in DC mode and is compact enough to reach the full magnetic field within approximately one week.

The solenoid for the P^3 experiment serves as a prototype for a potential FCC-ee positron production magnet in several key aspects: room temperature bore aperture (72 mm diameter), bore magnetic field strength (15 T), and the suitability of its mechanical and thermal design. For the P^3 experiment, the anticipated radiation exposure of the cold mass is significantly lower compared to FCC-ee conditions, both in terms of dose (18 kGy vs 23 MGy per year) and displaced atoms (10^{-8} vs $2{\cdot}10^{-4}$ DPA per year), even though these FCC-ee estimates include tungsten shielding [10]. Therefore, P^3 will not address potential radiation damage to the superconductor. The available space for shielding inside the 72 mm diameter bore is approximately 16 to 20 mm per wall.

The decision to construct the solenoid from five identical coils, without including compensation coils to shape the magnetic field, resulted from several design iterations that balanced yield with simplicity. Although a higher yield configuration might be achievable for FCC-ee with a more complex winding pack, the expected gains are minimal [12]. For a detailed discussion on the magnetic field profile optimization, the interested reader can refer to [4, 12, 13].

The assumption that the target can be stationary and thus inserted inside the solenoid is realistic due to the reduced power load on the target, thanks to the high yield. By being able to place the target inside the bore, a large fraction of the decay tail of the magnetic field can be utilized to capture the generated particle shower. The exact optimum target location depends on the beam parameters [3, 4]. For P^3, a placement at the 12.7 T point is selected [2].

Most concepts that will be used in the P^3 solenoid were successfully tested at PSI using an 18 T small-bore test coil solenoid program. This program addressed coil winding, soldering, stacking, and electro-thermal concepts related to conduction-cooled operation at high current (2 kA). The 18 T program benefited from a licensing agreement with tokamak energy concerning their NI technology. The P^3 solenoid will use tokamak energy's technology for axial current injection. The soldering method employed relies on PSI in-house developments. Two major system-level differences compared to the 18 T solenoid are the presence of a warm bore for P^3 and, for quench prevention, the addition of heat capacity in the form of a solid

Table 1. P^3 solenoid magnet parameters.

Coil type	Single pancake two co-wound tapes ReBCO sides facing	
Number of pancakes	5 (+1 spare)	
Winding pack inner radius	61	mm
Winding pack outer radius	109.5	mm
Axial coil spacing	1.0	mm
Tape width	12	mm
Unit cell thickness	63±5.7	μm
Turns/coil	385	
Tape length/coil	412 (2·206)	m
Current	1.2	kA
Stored energy at 1.2 kA DC	348	kJ
Inductance at 1.2 kA DC	0.484	H
Time constant L/R at 15 K	∼13	h
Minimum charging time (>7 tau)	>4	d
Operating temperature	15	K
Bore field at 1.2 kA	15.2	T
Max field on conductor at 1.2 kA	$\|B\|$ 21.0	T
	$B\|\|$ 21.0	T
	$B\|-$ 12.1	T
0.5 mT line at 1.2 kA	Between $(r,z) = (0,2.9)$ and (2.1,0)	m

buffer. All major components have arrived in the assembly space, including the cryostat, radiation shield, cryocoolers, and 2.8 km of 12 mm ReBCO tape. Coil manufacturing started in Q3 2024 and complete system tests are anticipated in Q1–Q2 2025. Table 1 shows the main P^3 magnet parameters.

The structure of this work is as follows: first, an overview of the magnet system is given. Second, electro-thermal design aspects are discussed. Finally, mechanical simulation results are presented.

2. System overview

This section gives a brief overview of the major system components, after which these sub-components are presented in more detail. The cold mass primarily consists of a NI ReBCO solenoid composed of 5 pancake coils (see figure 2). This stack is essentially a scaled-up version of the 18 T-bore-field test coil stack (compare figure 5), manufactured and tested at PSI between Q4 2021 and Q2 2022. For the P^3 experiment, the inner and outer diameters of the test coils will be scaled from 50/100 mm up to 122/219 mm, respectively (see table 2). The cold mass will be conduction-cooled in a cryogen-free cryostat (see figure 2) by two single-stage cryocoolers (Sumitomo RDK500B). One cooler is used for the cold mass, while the other cools the radiation shield and the current leads.

The five single-pancake coils are placed between two 6 mm thick copper plates, which function as current terminals and allow the current to enter the coils axially. To provide cooling,

Table 2. Radial build. The magnet features room for radiation shielding, which would be needed for FCC-ee operation.

Component	r_i (mm)	r_o (mm)
Warm bore	0	36
Room for FCC-ee tungsten shielding	16–20	36
Inner stainless steel wall	36	38
3 MLI 10-layer blankets (3 mm/blanket+vacuum)	38	52
Inner radiation shield	52	54
Vacuum	54	58
Winding pack	61	109.5
Stainless steel overbanding	109.5	129.5

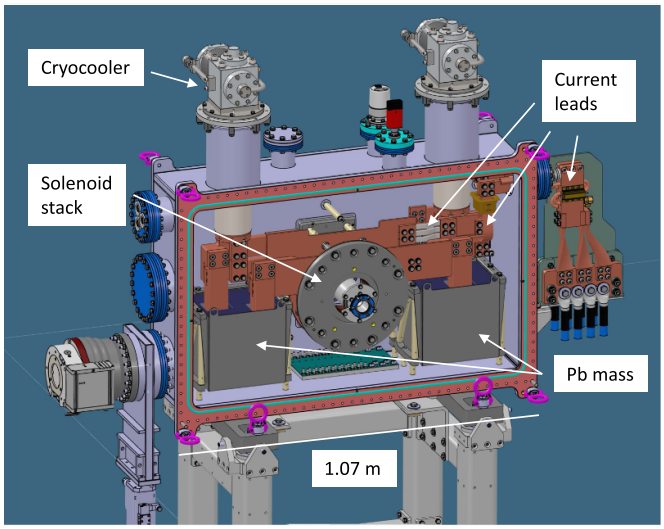

Figure 2. P^3 cryostat. The cryostat downstream wall, thermal shield and MLI blankets are not shown.

the plates are connected via flexible copper links (RRR[1] ∼67) and an electrically insulated interface to the cryocooler (see figures 2 and 3).

On the axial outer side of either copper plate, two Teflon-coated stainless-steel plates are attached. These plates hold the cold mass together, as they are connected by bolts. The cold mass is held in place by a support structure made of G10 and stainless steel, which connects to the downstream stainless steel flange, see figure 4.

The operating current is 1.2 kA, supplied via leads that include both, a metal and an HTS section. These leads are sized for currents of 1.2 kA (metal section) and 2 kA (HTS section).

2.1. Pancake coils

The P^3 single-layer pancakes will be co-wound from two face-to-face pre-tinned ($Sn_{60}Pb_{40}$, 5 μm) 12 mm wide YBCO

[1] RRR is the Residual Resistance Ratio, and is the ratio of the resistance at room temperature (or sometimes 0 °C) relative to that at cryogenic temperature (4.2 K or 20 K) [14].

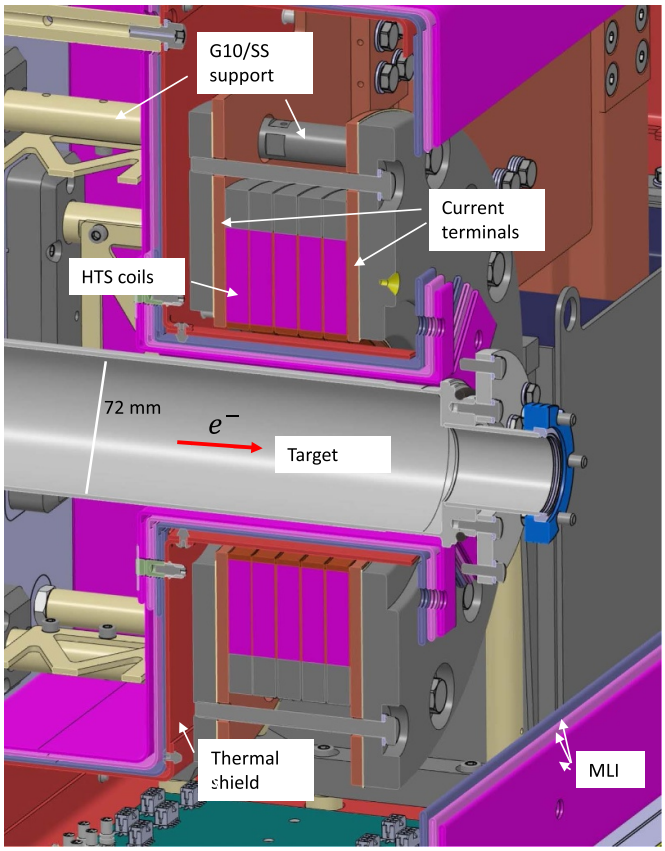

Figure 3. Zoomed-in view of cold mass. Part of the thermal shield and MLI blankets are not shown.

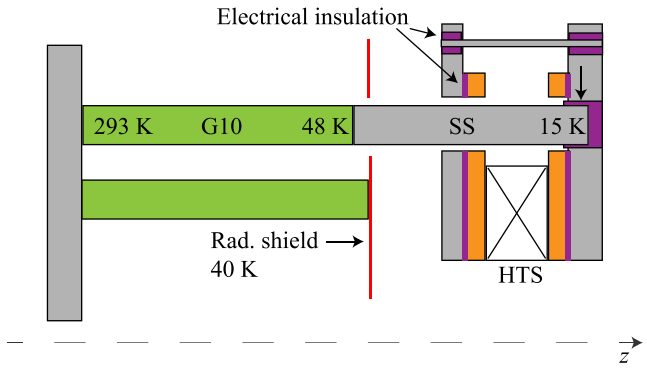

Figure 4. Sketch of support structure concept.

tapes, supplied by Faraday Factory Japan. The tape has a 38 μm substrate and 5 μm of copper stabilizer per side. The required length is 412 m per pancake (2·206 m).

During the winding, soldering flux is applied using a *flux foamer* [15]. After post-mortem analysis on several dummy pancakes, GSP-2533 flux (resin, low halides, organic, produced by Gie-Tec) was chosen for its ability to leave no observable residue and withstand the relatively slow heating of the winding pack towards soldering temperatures. Some pancakes feature internal splices, made by soldering.

Several turns of high-tension titanium tape are wound around the HTS tapes to prevent gaps from opening during the soldering process. The last titanium turn is spot-welded to keep it in place.

After a complete pancake is wound, it is dipped in more flux and placed in a vacuum environment. After the degassing of the flux, the probe holding the pancake is heated to 200 °C, followed by dipping the pancake into a 220 °C $Sn_{63}Pb_{37}$ bath for two minutes. Even though the solder's melting point is lower, 183 °C, raising the temperature significantly above the melting point enhances wetting and spreading ability [15]. The absence of an oxygen-containing atmosphere further benefits the soldering process. After the two minutes, the pancake is lifted from the bath, and the probe's heater is stopped. After the probe's temperature drops below 170 °C, the vacuum is broken to aid cool-down via convection. During the soldering operation, the pancake is above 200 °C for around three minutes.

2.2. Complete coil

After solder-potting, the titanium tape is removed. Each pancake is reinforced by winding stainless steel tape under high tension around the winding pack, a common technique for high-field solenoids [16–18]. This technique reduces the hoop stress in the superconductor caused by Lorentz forces. Using individual *overbanding* for each pancake is preferred over a single outer cylinder covering all pancakes, to avoid shear stress between the cylinder and the pancakes due to axial Lorentz forces. The overband has a radial thickness of 20 mm and is wound with 120 MPa winding tension. This corresponds to 200 turns of 0.1 mm stainless steel tape wound with 144 N tension.

As the final step in coil manufacturing, the current lead plates are attached. Current is fed into the coils using axial joints (figure 5), using tokamak energy's electrothermal interface concept [19]. The axial joints rely on contact over several (∼14) turns, which may make this contacting method less suitable for high-precision magnetic field applications, as the current path depends on the realized contact. However, advantages include robustness and ease of pancake stacking. To ensure parallel surfaces, the outer flat surfaces of the plates are milled after their attachment to the coils.

2.3. Coil stack

To assemble a solenoid from individual pancakes, the pancakes and the copper terminal plates are stacked. Unlike the small-scale demonstrator, where pressed contacts were used to stack pancakes together (∼50 nΩ per connection), the P^3 pancakes will be soldered to each other and to the copper end-flanges using Field's metal. Its low melting point of 62 °C [20] allows disassembly of the stack without desoldering the pancakes themselves. Initial soldering tests with an ORM1 type flux (95% water, 5% glutamic acid hydrochloride) show decent wetting and bonding.

The terminal plates have to be electrically insulated from the support structure. This is primarily achieved by employing

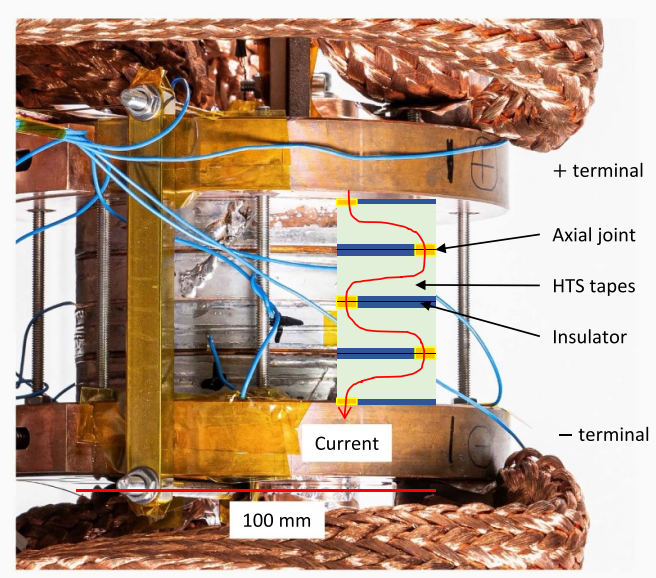

Figure 5. 18 T 4-pancake stack, with current terminals attached. The copper braids have a dual function: they are both current leads and heat drains. The schematic shows how the current is injected and extracted using axial joints.

bushings as isolation between the support structure's stainless steel rod and downstream stainless steel plate, see figure 4.

Additionally, the interface between the copper plates and stainless plates is designed to have low friction. If a rigid connection between the copper and stainless steel would be used, e.g. by using epoxy, this would result in high axial compression of the coils during their powering, as the stainless steel plates would prevent the coils from axially deforming towards the center plane. To avoid this, instead a low friction interface is used, achieved by applying a Teflon coating on the stainless steel plates. A secondary benefit of this coating is an additional electrical insulation layer between the coils and the rest of the system. The expected friction coefficient between copper and Teflon at cryogenic temperatures is between 0.1 and 0.5, depending on factors such as temperature and copper surface roughness [21, 22]. The stainless steel plates are connected to each other by six electrically insulated stainless steel M8 bolts. The axial thermal contraction of the stack, including the copper flanges, is 0.269%, so stainless steel bolts (0.296% [14]) can be used without loss of pre-compression during cool-down. The bolts are tightened to 8 kN each and gain an extra 2 kN during cool-down, resulting in a total compression force of 60 kN. A 5 kN axial compression on the stack is sufficient to prevent the winding pack from moving due to gravity, assuming a friction coefficient of 0.1. The remaining clamping force can prevent the winding pack from moving in case some net magnetic force is exerted on the coils in the *xy*-plane, up to a maximum of 5 kN.

2.4. Support structure

The cold mass is secured in place by a support structure that attaches it to the upstream cryostat wall (figure 3). A downstream supporting structure is omitted due to limited space in this area, driven by the desire to minimize the distance between the solenoid and the downstream RF structures. The structure comprises eight pillars. Each pillar, see figure 4, is made from a G10 section in series with a stainless steel section. The G10 part is connected to the cryostat wall, and the stainless steel section is connected via electrical insulation to the downstream steel plate of the cold mass. The pillar structure passes through holes in the radiation shield, the upstream stainless steel flange, the upstream copper terminal flange and the downstream copper terminal flange, without making contact.

Constructing the support structure from these two components ensures that the temperature drop (293 K to 50 K) mainly occurs over the G10 section. Thus, radiation emitted from within the radiation shield is reduced, albeit with an acceptable increase in conductive heat load compared to a full G10 solution.

Apart from gravity, the primary unbalanced force on the cold mass is the attraction towards the downstream normal conducting solenoids, estimated to be up to 30 kN. By not connecting to the upstream stainless steel flange, we increase the thermal pathway and prevent magnet-magnet attraction from creating tensile axial stresses between the coils. With this solution, stress is compressive on the coils and tensile on the support. An additional benefit is that many interfaces experience compressive rather than tensile stress due to magnet–magnet interaction, including the coil/coil, coil/copper flange, and copper flange/downstream stainless flange interfaces.

2.5. Thermal buffer

Instead of relying on quench protection for this system, we aim to prevent quenches[2] from developing following fault scenarios. There is no protection foreseen for this magnet for cases in which a quench occurs in the windings. To avert quenches during normal operation, the system operates with a large enthalpy margin (the minimum quench energy is 12 J).

In the event of a fault in the current leads, power supply, or cryocooler, the system must safely ramp down the magnetic field. To achieve this, two 115 kg lead blocks serve as a thermal buffer due to their substantial heat capacity. These blocks are connected to the cold mass and its cryocooler with flexible copper braids. Lead was chosen due to its large heat capacity per volume [14] at operating temperature, and is a typical choice when additional heat capacity is desired [23]. Neon would have been a valid option as well.

The worst-case scenario involves a complete power failure, resulting in the loss of cryocooler- and power supply operation. In this scenario, all stored magnetic energy dissipates inside the cold mass through the radial path formed by the NI coils' solder. A switched-off RDK500B coldhead will conduct a heat load of around 13.5 W through its neck [24].

[2] Here we define a quench in a conduction-cooled NI magnet as a monotonic decrease of the central bore magnetic field in time, together with a non-monotonic increase in time of the warmest point in the winding pack. This definition only works for operational phases in which the operator is not actively manipulating the system.

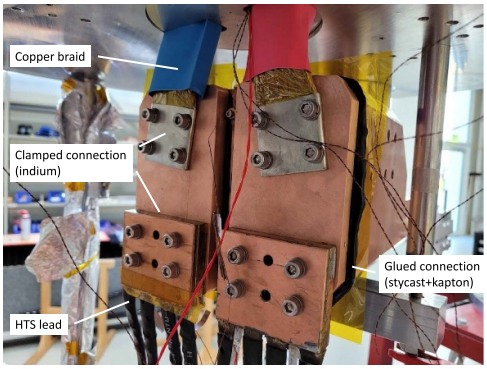

Figure 6. PSI test-stand current lead thermalization. Flexible metal current leads (red and blue) carry a current of 2 kA from room-temperature to the thermalization plate. The thermalization plate is connected to a copper block that is itself connected to the cryocooler via a bolted connection with thermal grease. HTS leads (black) are also connected to the thermalization plates.

Without the thermal buffer, the rise in temperature would be fast relative to the decrease of magnetic field, and a quench would develop. Calculations on this scenario are presented in the next section. Due to relatively large timescales involved, the heat capacity is situated some distance (0.24 m) away from the solenoid itself. This contrasts with efforts to enhance Nb_3Sn heat capacity by adding high-C_p material near or even inside the strands [25, 26].

2.6. *Intermediate temperature stage and interfaces*

The second RDK500B cooler is dedicated to cooling the radiation shield and the metal current leads. The shield is made from 2 mm thick aluminium (type EN AW-1050) and has a surface area of 1.5 m^2. Three blankets of multi-layer insulation (MLI), each comprising ten layers, are placed on the room-temperature facing side of the shield. Seven G10 pillars provide mechanical support for the shield.

The current leads consist of two sections: a low-RRR copper braid transfers current between room-temperature and the intermediate temperature heat-sink, and an HTS section facilitates current flow between the heat-sink and the coils. The metal leads' cross-section is optimized following the approach in [27].

Removable, electrically conductive, joints are made by bolting surfaces with a 100 μm indium sheet in between. Titanium washers are utilized to prevent a loss of pre-tension due to differential thermal contraction.

Thermalization is achieved through copper pads connected to the cryocooler via an insulated connection, similar to the PSI test coil setup (figure 6), using a glued copper/stycast/kapton (50 μm)/stycast/copper interface. The measured thermal contact resistance (TCR) of such an interface is presented in table 3. In the experiment, a copper base-plate attached to a cryocooler was set to the desired temperature by means of a PID-controlled heater and a temperature sensor. A smaller second copper plate (surface area around 9 cm^2) was attached to the main plate via the mentioned interface of stycast and kapton. The smaller plate also contained temperature sensor and a heater to create a temperature gradient of around 2 K across the interface. The TCR could then be calculated from the temperature difference between the copper plates and the supplied heater power.

Table 3. Thermal contact resistance of copper/stycast/kapton (50 μm)/stycast/copper.

T (K)	TCR (mKm^2 W)
10	1.78
20	1.00
30	0.80
40	0.74
45	0.72
50	0.73
60.5	0.75

Although a sapphire interface could potentially allow the same TCR with a smaller cross-sectional area [28], the chosen approach offers robustness by avoiding the use of brittle sapphire clamped connections.

The HTS leads are made from six 12 mm tapes each, separated in three stacks of two tapes to mitigate the influence of the self-field on the current-carrying capacity. The tapes are enclosed in a glass-fiber sleeve and a perforated heat-shrink tube. After soldering the tapes to the copper terminals, the leads are submerged in a container of molten wax. This method provides some mechanical support while still allowing flexibility during installation using a hot air gun. The maximum Lorentz force on a stack of two tapes is 14 N.

3. Electromagnetic-thermal simulations

In a conduction-cooled cryocooler-based system, the operating temperature and electromagnetic behavior are interconnected. Therefore, we estimate the solenoid's performance using a coupled approach, considering the system's response to different applied current levels to assess available margins.

These simulations will be repeated once time-constant measurements of the first P^3 winding packs and the full coil will be available. This will determine if the thermal buffer remains sufficient to ensure safe operation at 1.2 kA with a margin (a safe discharge up to 1.4 kA is the design target).

The cold mass electromagnetic and thermal behaviour is simulated in COMSOL using a 2D axisymmetric homogenized geometry based on an H-formulation model, similar to that in [29]. The main innovation in [29] is the inclusion of the tapes' spiral path by means of off-diagonal terms in the resistivity matrix.

The $I_c(B,T,\theta)$ behaviour of the tape is taken from [30, 31] and represents SuperOx YBCO tape[3]. A scaling law proposed by [32] is used. The fitted I_c is multiplied by 0.95 to take into account a potential 5% I_c-degradation due to the soldering processes. This is thought to be conservative [33]. An $E = E_c(J/J_c)^n$ power law is used to calculate the electric field, where the exponent n is parameterized by fitting $n(I_c)$ data

[3] Tape with similar performance is obtainable from Faraday Factory Japan.

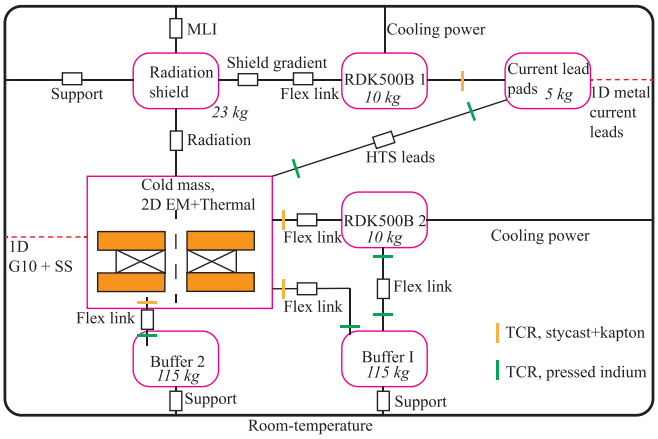

Figure 7. Lumped thermal network. Nodes (masses) are connected via resistances (thermal connections). Some of these resistances (the support structure and the metal current leads) are simulated as 1D objects.

at 15 K, as motivated by [34]. n ranges from 15 to 60 [30], depending on J_c.

The test-coils' performance is used for an estimation of the expected time constant of the P^3 coils. A fit of the form

$$\rho_r\,[\Omega\cdot\mathrm{m}] = 5.7\cdot10^{-13}T + 11.2\cdot10^{-11} + 3.3\cdot10^{-13}B \quad (1)$$

represents the turn-to-turn resistivity ρ_r. With an estimation of the P^3 solenoid inductance of around 0.5 H, an effective time constant τ of approximately 13 h at 15 K is calculated. This implies a minimum charging time of $7\tau = 4$ d, if the power supply current were ramped as a step function. In practice, a slow ramp is used to prevent significant heating in the radial current path.

Material properties, besides the turn-to-turn resistivity and the scaling law of the superconductor, are mainly taken from [14]. The resistive domains of the current lead plates are given a thermal conductivity of 2 W m^{-1} K^{-1} via a rule-of-mixture estimate based on their inner structure. Thermal properties of the winding pack are computed using the (inverse) rule of mixtures, assuming RRR = 20 for the copper's temperature and magnetic field dependent thermal conductivity [35].

The copper terminals link to a lumped thermal network representing the cold mass, the coolers, and their interfaces. The network is sketched in figure 7. The radiation shield receives a heat load through the MLI, considering both conductive and radiative contributions [36]), and through the shield's support structure. The shield connects to one of the cryocoolers through a flexible copper link in series with a resistor that represents the thermal gradient across the heat shield. This gradient is estimated through a 2D FEM simulation, with the thermal conductivity of type 1050 aluminum obtained from [37]. The combined thermal resistance of the copper link and the shield is set to 3.5 K W^{-1}

The metal leads are simulated using a 1D coupled heat transfer-electrical current model. The cross-section of the current leads is adjusted for each maximum current scenario, with, for instance, the 1.8 kA scenario requiring a 50% larger cross-section than the 1.2 kA one.

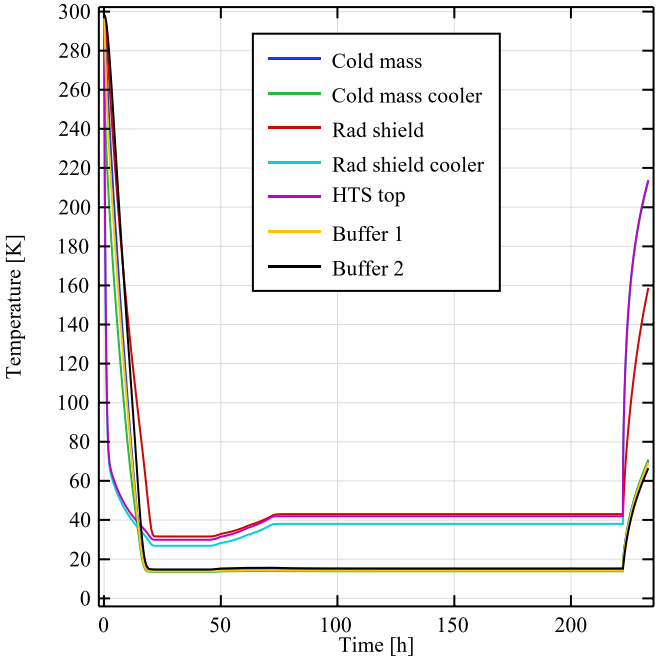

Figure 8. Temperature profile of several major system components. Shown are cool-down, ramp, and fault, for 1.2 kA scenario.

The simulations capture the system's cooldown, subsequent energizing, and magnetic field stabilization phases. Following stabilization, a fault scenario is introduced wherein a power failure halts the power converter and cryocoolers. Consequently, all stored magnetic energy must dissipate within the cold mass.

3.1. Temperatures and heat loads

According to the simulation results, the system requires approximately one day to cool down (figure 8). Once stabilized after ramping to 1.2 kA, the coil's temperature is around 15 K. During the ramp, the temperature of the radiation shield begins to rise. This is because the cooler connected to the shield has to cool away the increased load coming from the metal current leads. However, the increased thermal radiation from the shield to the cold mass due to the shield becomes warmer is not significant enough, see table 4, to raise the cold mass temperature. Additionally, the dissipation within the cold mass itself is relatively modest compared to the total heat load seen by the cold mass' cooler.

The observed heat load on the cold mass (10 W) may seem substantial, especially when considering that typical MRI systems operate at 4 K using a 1 W cooler [38]. However, further optimization of the heat load would only marginally enhance the system's performance at 1.2 kA. The RDK500B cooler delivers a cooling power of 0.5 W at 13 K and 10 W at 14 K [39], resulting in a maximum potential improvement of only around 1 K.

The largest temperature difference on a component interface, 4 K, is across the insulated thermal contact between current lead and cryocooler (see figure 6). This is followed by the

Table 4. Heat loads after ramping to 1.2 kA.

	Cold mass (W)	Intermediate stage (W)
MLI		2.2
Support for rad. Shield		1.5
Copper current leads		104
Radiation	0.02	
Dissipation in coils	0.25	
Dissipation in joints	2.1	
Buffer supports	2.6	
G10/SS supports	2.7	
HTS leads	2.1	
Total	9.8 at 14 K	108 at 40 K

connection between the cold mass cooler and the cold mass itself (0.5 K), and by the connection from the cold mass to the buffer (0.2 K).

3.2. Electromagnetic-thermal behaviour during fault

To get an idea of how the system behaves at different current levels, and from that estimate the available margins at 1.2 kA, a sweep over the maximum current supplied by the power supply was conducted. Figure 9(a) shows this current as a function of time. The two-cooler configuration enables ramping up to 2.2 kA, whereas 2.3 kA results in a thermal runaway and subsequent quench (figure 9(b)).

The central bore magnetic field over time for various currents is shown in figure 9(d). At the nominal operating current (1.2 kA) it takes approximately one week to ramp to a constant magnetic field of 15.3 T. The magnetic field at 1.2 kA at the cryocooler's cold finger has a maximum value of 0.10 T and at the motor stage, it reaches 10 mT. These values fall below the recommended limits of 0.3 T and 30 mT, respectively [40].

The highest attainable central bore field is 17.5 T, achievable at 1.5 kA. At higher currents, the increased radial current raises the temperature due to dissipation. Consequently, this reduces the superconductor's current-carrying capacity and thus the generated field.

While the coils can handle currents of up to 2.2 kA when the leads are properly scaled, the magnet cannot sustain such high currents during a fault scenario without quenching.

After initiating the fault scenario in the simulation, the cooling power is disabled, and heat leakage through the coolers' necks is introduced. Additionally, the electrical circuit is opened (i.e. forced to zero current) on the room-temperature side. Consequently, the coils begin to heat up (figure 9(c)) with a heating rate dependent on the current carried when the fault starts, as the current is forced through the radial path.

If the initial current is 1.5 kA or lower, the stored energy dissipates slowly in the cold mass over several hours. At 1.6 kA, a quench develops in the coils after 15 min (as seen by sharp temperature spikes in figure 9(c) and magnetic field drops in figure 9(e), following an initial gradual temperature increase. For even higher currents the quench occurs within minutes after the start of the fault. The first few seconds after the fault begins involve a dip in temperature over around one minute, caused by the disappearance of joule dissipation in several joints.

The simulation was repeated for various cold mass weights, and figure 10 was generated from the results. At the nominal operating point of 15.2 T the stored magnetic energy is 348 kJ. With an installed lead buffer of 230 kg (total cold mass weight 281 kg), the stored energy per kg of cold mass is 1.23 kJ kg^{-1}. The simulation predicts that a reduction of the cold mass of a factor 3, and thus an equivalent increase in the stored energy per kg, would lead to a quench during an open circuit at 1.2 kA. Thus, there is significant margin present.

The next section will discuss the mechanical behaviour of the magnet under nominal 1.2 kA operation.

4. Mechanical simulations

This section begins with mechanical simulations on the cold mass, followed by an estimation of the attraction force between the HTS solenoid and the downstream 0.4 T NC solenoids. Finally, the support structure holding the cold mass in place is analyzed to determine the displacement of the coils relative to the beam-pipe.

As shown in figure 3, the cold mass consists of five pancakes, stainless steel overbanding, two large copper flanges on top and bottom of the pancake stacks that act as the electrical and thermal terminals, and two Teflon-coated stainless-steel flanges.

The copper flanges, due to soldering to the winding packs, must handle a significant part of the radial Lorentz force from the adjacent pancake. Therefore the chosen alloy is a compromise between conductivity and mechanical strength. Half-hard copper Cu-OF (EN 13 599-CW008A) has a high yield strength (330 MPa at 4 K [41]). For the simulation, the copper's non-linear stress strain curve above 330 MPa is taken from [41].

Interfaces are either soldered (coil/coil and coil/copper flange), high (1.0) friction (coil/overbanding) or low (0.5) friction (copper flange/Teflon).

For the smeared properties of the current lead plates attached to either side of every coil, a rule-of-mixtures estimate yields $E_r = E_\phi$ =100 GPa, E_z =29 GPa.

4.1. Mechanical simulation set-up

The initially considered approach was to simulate the cold mass as a whole, with the winding pack treated as an orthotropic homogeneous material, followed by a sub-scale model in which the winding pack composition is explicitly modeled.

Using an orthotropic homogeneous bulk has been shown for Nb–Ti-based epoxy-impregnated winding packs to accurately describe the composite's behaviour [42, 43]. To translate the results from the smeared winding pack to the stresses in its components, a sub-scale model would be made in which the

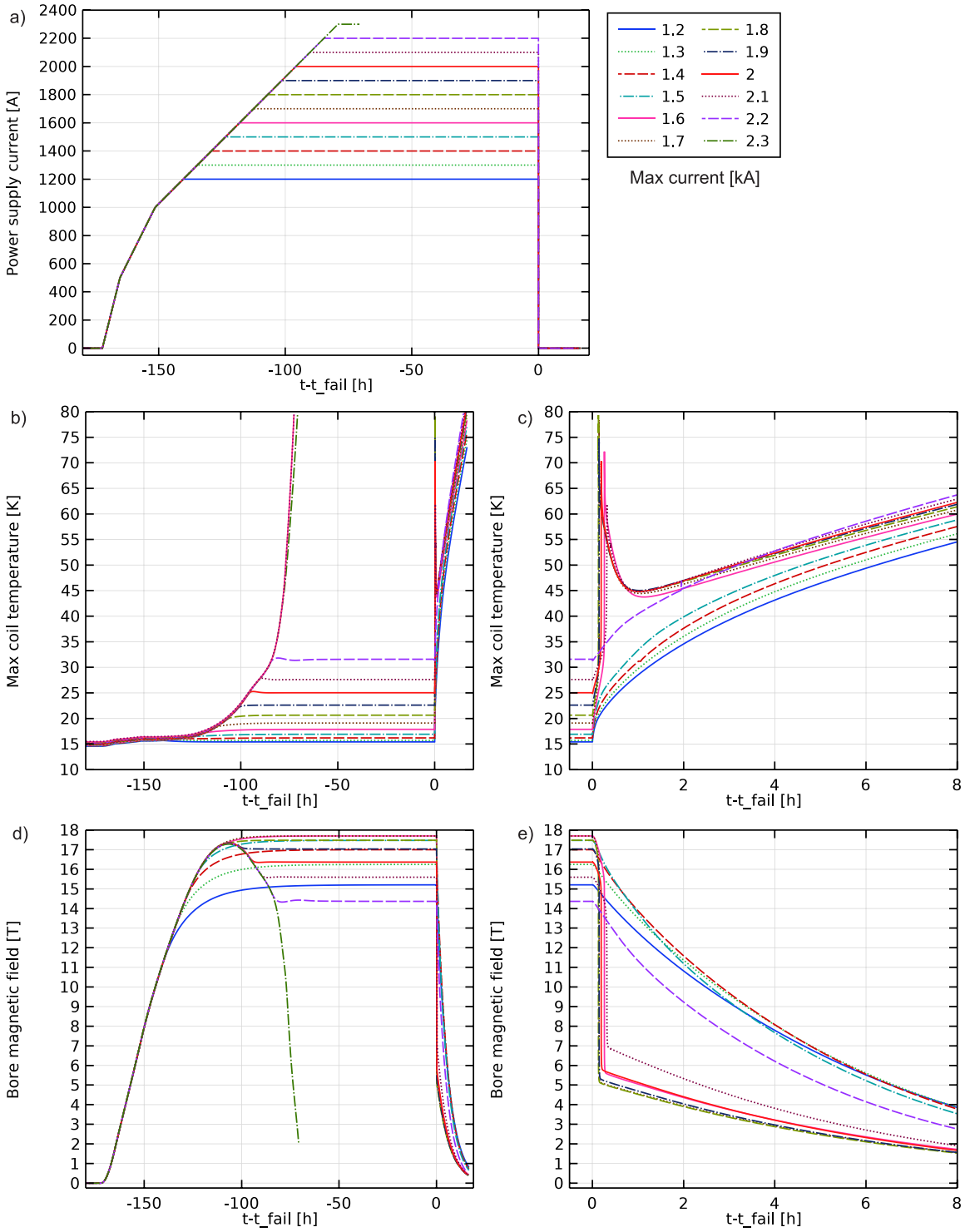

Figure 9. a) Power supply current as a function of time, for different maximum operating currents I_{supply}. (b), (c) Maximum coil temperature versus time. (d), (e) Magnetic field in center of the bore. The cryocoolers are stopped at the time t_{fail}, and an open circuit is introduced.

displacements of the full-scale model are given as boundary conditions, similar to the approach in [44].

However, this method has limitations. It cannot fully capture stresses due to differential thermal contraction, as the tape and solder have different stress-free reference temperatures. Additionally, modeling plasticity of constituent materials is challenging with an orthotropic homogeneous bulk stiffness matrix.

Therefore, the chosen analysis method explicitly models the tapes, see figure 11. To keep the simulation manageable, the thickness of the tapes is increased by a factor 10, while the number of turns is reduced by the same factor. So, each

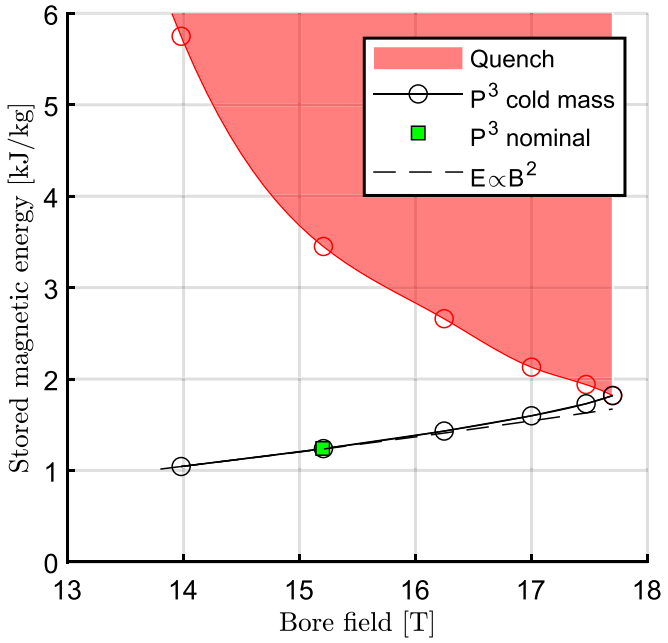

Figure 10. Stored magnetic energy per kg of cold mass versus bore magnetic field, during stable operation. The black markers/spline indicate the relationship between stored energy and the bore magnetic field for the P^3-configuration. The red area indicates configurations where the maximum allowable deposited energy density is exceeded for a given magnetic field. This means that in this region a quench would occur after the power supply is interrupted.

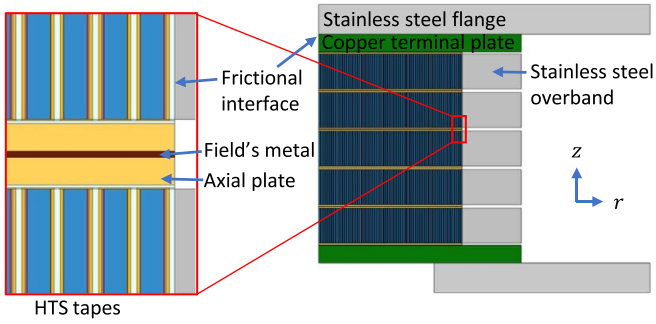

Figure 11. Mechanical simulation geometry.

pancake, instead of having 770 (385 × 2) turns of 63 μm tape, has 77 turns of 630 μm tape. The silver [45], copper [46] and PbSn [47] are given non-linear stress–strain curves.

The simulation is done in COMSOL and uses the Activation feature, which allows to activate domains at desired steps in the solver. For example, the stainless steel flanges are not physically there during the solder process, so these are disabled in the first solver steps. 'Disabled' here means that the effective Young's modulus is multiplied by 10^{-5}. Materials are activated in a stress-free state by removing elastic strains at the moment of activation.

The solver sequence used is as follows:

- The winding tension is applied. No constraints are applied to the outer surfaces. Rigid motion suppression is used to prevent rigid movement in the z-direction.
- The titanium overbanding is applied under tension.
- Soldering of the coils at 183 °C. The tape's constituents are given a stress-free reference temperature of 20 °C. The tapes are allowed to expand as the solder is initially not activated. After the tapes have expanded, the solder is activated. The stress-free reference temperature of the solder is 183 °C.
- The current lead plates are attached (activated). In reality, this happens at a separate 183 °C soldering step. The intermediate cool-down to room temperature is not considered here.
- The winding pack is cooled down to 20 °C. The titanium overband is replaced by stainless steel overbanding is activated, followed by applying the winding tension to the overbanding. To account for the complex non-linear compressive behavior of the dry-wound overbanding [48], the radial modulus of the steel is set to 1/3 the bulk value.
- The collapsible winding mandrel is removed.
- The coils are heated to 120 °C. The Field's metal between coils is activated, as are the outer copper flanges which form the solenoid's current leads.
- The stack is cooled to 20 °C, and the stainless steel flanges are attached (i.e. activated).
- The stack is cooled to 15 K.
- The coils are energized: the Lorentz force is applied, as is the attraction force towards the normal conduction solenoids (30 kN) and cryostat lid (2 kN).

4.2. Winding pack stresses

The stress analysis indicates that the Hastelloy substrate experiences a hoop stress of 450 MPa and a von Mises stress of 580 MPa at the innermost turns of the middle coil. Without the overbanding, the maximum hoop stress would increase to 500 MPa. These values are well within the tensile strength limits of ReBCO conductors, with Hastelloy substrates capable of handling up to 800 MPa stress [49].

The minimum radial stress, representing compressive stress perpendicular to the tape's flat face, is −155 MPa. This value is also within acceptable limits, as the compressive strength of ReBCO conductors typically exceeds 300 MPa [50]. The delamination strength of ReBCO conductor below 77 K can be above 10 MPa [51–53], though values as low as 4 MPa have been reported [54]. The predicted maximum radial stress, located at the innermost turns (figure 12(c)), is 2 MPa. Increasing the winding tension of the overband does little to decrease the radial stress at this location. Avoiding positive radial stress entirely would require a smaller ratio of outer-to-inner coil radii [27], or nesting of coils. So a slight risk of some delamination is present in the current design.

A too high axial compressive stress can damage the winding pack. Measurements on NI winding pack without solder impregnation made from ReBCO tape with a 50 μm substrate and either 20 μm or 40 μm total copper thickness show I_c-degradation above stresses of 230 MPa and 200 MPa respectively [55]. Assuming the maximum allowed stress to scale with the substrate: non-substrate ratio yields an upper axial compressive stress limit of 215 MPa for the P^3 arrangement. The estimated axial compressive stress is highest at,

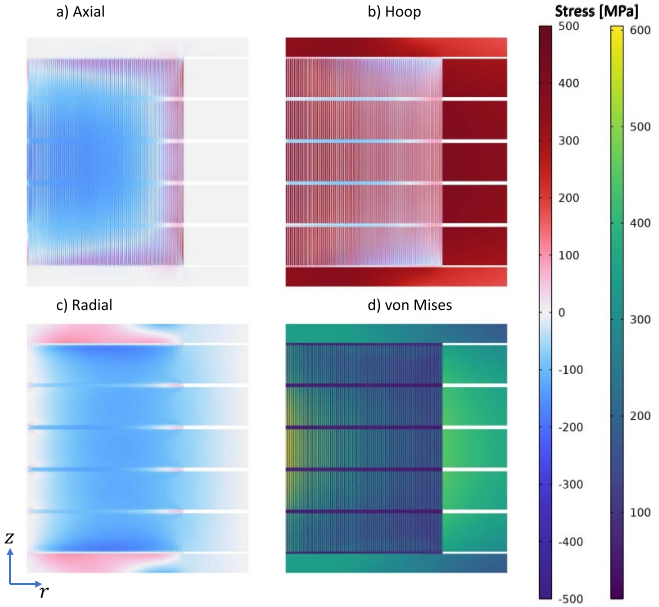

Figure 12. Stresses after energizing. (a) Axial stress, (b) azimuthal stress, (c) radial stress, (d) von Mises stress.

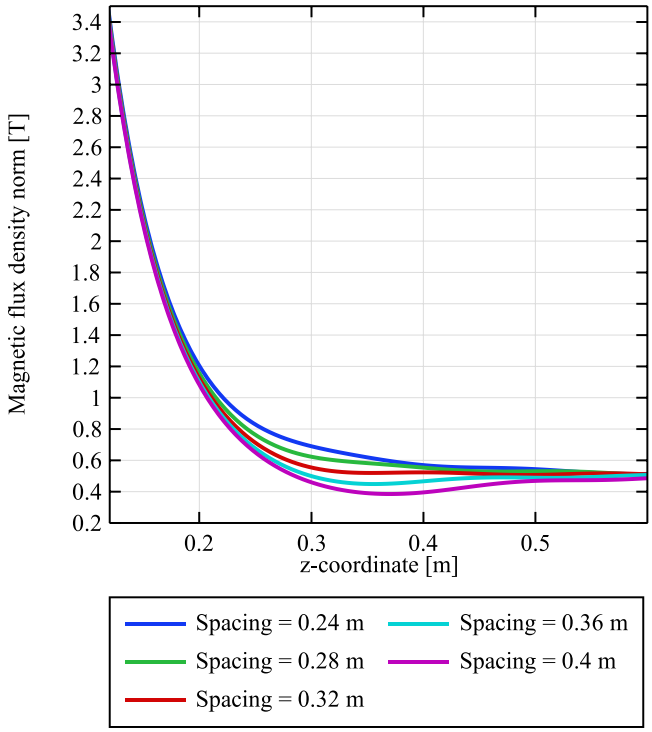

Figure 13. Magnetic field profile on axial center line around cross-over region between the HTS solenoid and the downstream solenoids, for several different separation distances between them.

again, the innermost turn of the middle coils, and is 139 MPa averaged over the tape, or 150 MPa if the solder is included.

Concerning the solder connection between tapes, the tensile strength of a PbSn/Cu bond is greater than 110 MPa at 100 K [56], but brittle failure might occur at lower temperatures [57]. The maximum tensile stress experienced by the solder in the radial direction is 2 MPa. In the axial and azimuthal directions, the solder is in compression. So in case perfect solder contact were to be achieved, the stresses would be at acceptable levels.

There is the possibility that, if the soldering operation leaves voids, stress concentrations can start local ReBCO delamination, even with moderate overall radial stress. In this case we rely on the intrinsic stability of NI coils which provides alternative current paths in case of local damage.

The estimated peak stress on the Field's metal, used to solder coils to each other, is 75 MPa, and is present already after cool-down due to differential thermal contraction. The Field's metal, if unconstrained, is estimated using the rule of mixtures to shrink 0.57% [14]. Field's metal can handle ultimate shear and tensile stresses of 100 MPa and 170 MPa, respectively, at cryogenic temperatures [20]. This indicates that the stress levels in the field's metal are within acceptable limits.

4.3. HTS solenoid to RF solenoid attraction

The estimation of the attraction force between the HTS solenoid and the downstream solenoids around the RF cavities indicates a significant force, which depends on the separation distance between the systems. For the current design with a separation distance of 0.17 m, the estimated force is approximately 20 kN. This force is handled by the 8 G10/SS pillars (see figure 4. Moreover, the attraction force between the HTS solenoid and the downstream cryostat lid, made of annealed 316 L with a thickness of 30 mm, is estimated at 2 kN (lid susceptibility of 1.01).

The required distance between the normal conducting and superconducting solenoids follows from the magnetic field requirements. Ideally the magnetic field profile has a negative slope [12], $\mathrm{d}B/\mathrm{d}z < 0$ for $z > 0$, which is satisfied for separation distances shorter than 0.33 m, see figure 13.

4.4. Support structure

The displacement of the cold mass relative to the cryostat exterior is important for the positioning of the magnet with respect to the target and the beam.

The cold mass moves around 0.5 mm towards the upstream cryostat wall during cool-down, mostly due to contraction of the support structure. When a 30 kN force towards the downstream 0.45 T solenoids is applied, a movement of 0.1 mm in the axial direction is expected. The vertical displacement due to gravity is around 160 μm.

5. Further steps towards the FCC-ee capture solenoid

The described magnet is part of an effort towards an FCC-ee injector with a positron source based on an HTS magnet as an adiabatic matching device. The P^3 experiment aims for demonstrating several aspects of a high-yield source. While the 72 mm diameter bore has been sized to accommodate tungsten-based shielding based on initial radiation dose

simulations [10], it is not yet clear if more detailed design work on the target, its cooling path, and the shielding will necessitate a larger bore diameter for FCC-ee.

6. Conclusion

The proof-of-concept high-yield positron experiment at PSI, P^3, aims to make significant steps in exploring the potential of NI HTS technology for high-yield positron production experiments. For a compact DC application in which magnetic field *strength* is required, and not necessarily field *quality*, NI-HTS technology is a good solution. The capture solenoid is expected to operate safely at 15 T, 15 K, 1.2 kA, being conduction-cooled with two cryocoolers. The demonstrator system will be commissioned at the mid 2025.

In the event of external faults, the magnet's design ensures that the magnetic energy can be dissipated within the cold mass without triggering a quench. This resilience is enabled by the incorporation of additional heat capacity in the form of solid lead blocks.

Mechanical stress analysis reveals that the expected stresses experienced by the magnet's components, primarily arising from differential thermal contraction and magnet powering, remain below degradation limits.

Data availability statement

No new data were created or analysed in this study.

Acknowledgment

This work was performed under the auspices of and with support from the Swiss Accelerator Research and Technology (CHART) program (www.chart.ch).

We thank G Tomás, University of Twente, for the RRR measurements on copper samples.

ORCID iDs

Jaap Kosse https://orcid.org/0000-0003-2382-8495
André Brem https://orcid.org/0000-0003-2981-9880
Stéphane Sanfilippo https://orcid.org/0000-0002-3112-3463
Bernhard Auchmann https://orcid.org/0000-0002-3407-8864

References

[1] Craievich P 2022 The FCCee pre-injector complex
[2] Vallis N *et al* 2024 Proof-of-principle source for future colliders *Phys. Rev. Accel. Beams* **27** 013401
[3] Vallis N, Auchmann B, Craievich P, Duda M, Garcia-Rodrigues H, Kosse J, Schaer M and Zennaro R 2022 The PSI positron production project
[4] Zhao Y 2022 FCC-ee positron capture V0 simulation *FCC-ee Pre-Injector Mini-Workshop*
[5] Akai K, Furukawa K and Koiso H 2018 SuperKEKB collider *Nucl. Inst. Methods Phys. Res.* A **907** 188–99
[6] Mena Andrade R 2023 Design of the FCC-ee positron source target: current situation and challenges *FCC week 2023*
[7] Hahn S, Keun Park D K, Bascunan J and Iwasa Y 2011 HTS pancake coils without turn-to-turn insulation *IEEE Trans. Appl. Supercond.* **21** 1592–5
[8] Hahn S, Kim K, KIM K, Lee H and Iwasa Y 2018 Current status of and challenges for no-insulation HTS winding technique *TEION KOGAKU (J. Cryogenics Supercond. Soc.)* **53** 2–9
[9] Hahn S *et al* 2019 45.5-tesla direct-current magnetic field generated with a high-temperature superconducting magnet *Nature* **570** 496–9
[10] Humann B 2022 Radiation load studies for the FCC-ee positron source with a superconducting matching device *JACoW IPAC* 2879–82
[11] Fischer D X, Prokopec R, Emhofer J and Eisterer M 2018 The effect of fast neutron irradiation on the superconducting properties of REBCO coated conductors with and without artificial pinning centers *Supercond. Sci. Technol.* **31** 044006
[12] Zhao Y 2022 Optimisation of the FCC-ee positron source using a HTS solenoid matching device *Int. Particle Accelerator Conf. (13th)*
[13] Zhao Y 2021 Comparison of different matching device field profiles for the FCC-ee positron source *Int. Particle Accelerator Conf. (12th)* pp 2617–20
[14] Ekin J W 2006 *Experimental Techniques for Measurements* (Oxford U. Press)
[15] Manko H H and Rafanelli A J 2002 *Solders and Soldering* vol 124, 4th edn (McGraw-Hill)
[16] Raut P R, Bahirat H J and Atrey M D 2021 Analytical approach for optimal HTS solenoid design *IEEE Trans. Appl. Supercond.* **31** 1–9
[17] Gupta R *et al* 2011 High field HTS R&D solenoid for muon collider *IEEE Trans. Appl. Supercond.* **21** 1884–7
[18] Scott Marshall W S, Dixon I and Larbalestier D 2019 Design of strain-limited Bi-2223 insert coils for high-field magnets *IEEE Trans. Appl. Supercond.* **29** 1–4
[19] Brittles G, Kruip M, Langtry T and Smith G 2019 High temperature superconductor magnet US20220028591A1
[20] Yeh J T C 1984 Mechanical properties of In-based eutectic alloy solders used in Josephson packaging *Cryogenics* **24** 261–5
[21] Kensley R S and Iwasa Y 1980 Frictional properties of metal insulator surfaces at cryogenic temperatures *Cryogenics* **20** 25–36
[22] Bell R S, Kaferly Jones C and Fickett F R 1984 Copper-TFE friction at cryogenic temperatures *Cryogenics* **24** 31–35
[23] Yukikazu Iwasa 2009 *Case Studies in Superconducting Magnets: Design and Operational Issues* 2nd edn 223 (Springer) ch 4.5
[24] Euler A 2023 private communication *Sumitomo Cryogenics*
[25] Barzi E, Berritta F, Turrioni D and Zlobin A V 2020 Heat diffusion in high-C_p Nb_3 sn composite superconducting wires *Instruments* **4** 28
[26] Xu X, Li P, Zlobin A V and Peng X 2018 Improvement of stability of Nb_3Sn superconductors by introducing high specific heat substances *Supercond. Sci. Technol.* **31** 03LT02
[27] Wilson M N 1983 *Superconducting Magnets* ed N W Martin (Oxford University Press)
[28] Berman R and Mate C F 1958 Thermal contact at low temperatures *Nature* **182** 1661–3
[29] Mataira R C, Ainslie M D, Badcock R A and Bumby C W 2020 Finite-element modelling of no-insulation HTS coils using rotated anisotropic resistivity *Supercond. Sci. Technol.* **33** 08LT01
[30] 2021 Stuart Wimbush SuperOx YBCO 2G HTS

[31] Molodyk A *et al* 2021 Development and large volume production of extremely high current density $YBa_2Cu_3O_7$ superconducting wires for fusion *Sci. Rep.* **11** 2084
[32] Van Nugteren J and Danial M 2017 Parameterization of the critical surface of REBCO conductors from Bruker (available at: https://repository.cern/records/z5mzc-b0t43/preview/Bruker%20HTS%20Fit.pdf)
[33] Yazaki S, Karasawa A, Kotoyori T, Ishiyama A and Miyahara N 2013 Critical current degradation in high-temperature superconducting tapes caused by temperature rise *IEEE Trans. Appl. Supercond.* **23** 4602304
[34] Bang J, Kim K, Bradford G, Lee J, Abraimov D, Mato T, Noguchi S, Hahn S and Larbalestier D 2024 The effect of field-dependent n-value on screening current, voltage and magnetic field of REBCO coil *IEEE Trans. Appl. Supercond.*
[35] Hust J G 1984 Thermal conductivity of aluminum, copper, iron, and tungsten for temperatures from 1 K to the melting POINT National Bureau of Standards *Technical Report* NIST
[36] Ross R G 2015 Quantifying MLI thermal conduction in cryogenic applications from experimental data *IOP Conf. Ser.: Mater. Sci. Eng.* **101**
[37] Woodcraft. A L 2005 Predicting the thermal conductivity of aluminium alloys in the cryogenic to room temperature range *Cryogenics* **45** 421–31
[38] Atrey M D 2020 *Cryocoolers. Theory and Applications* (*International Cryogenics Monograph Series*) (Springer)
[39] SRDK-500B Cold Head Capacity Map (50/60 Hz), 2020.
[40] Kostrov E, Bagdinov A, Demikhov E, Demikhov T, Lysenko V and Piskunov N 2015 Performance test of a G-M cooler in magnetic field *Phys. Proc.* **67** 440–4
[41] Simon N J, Drexler E S, Reed R P, White R M and Lyons J W 1992 *Properties of Copper and Copper Alloys at Cryogenic Temperatures Technology Admlnletndlon.* (*National Inst. of Standards and Technology (Msel)* (CO (United States). Materials Reliability Div.)
[42] Ledbetter H M and Read D T 1977 Orthorhombic elastic constants of an NbTi/Cu composite superconductor *J. Appl. Phys.* **48** 1874–9
[43] Clark A F, Weston W F, Arp V D, Hust J G, and Trapani R J 1976 Characterization of a superconducting coil composite and its components *Technical Report* (National Institute of Standards and Technology)
[44] Daly M, Loffler C H D S, Fontenla A T, de Frutos O S, Guinchard M and Savary F 2018 Multiscale approach to the mechanical behavior of epoxy impregnated Nb_3Sn Coils for the 11 T Dipole *IEEE Trans. Appl. Supercond.* **28** 1–6
[45] Carreker R P 1957 Tensile deformation of silver as a function of temperature, strain rate and grain size *JOM* **9** 112–5
[46] Drexler E S, Simon N J and Reed R P 1992 Properties of copper and copper alloys at cryogenic temperatures. Final report No. PB-92-172766/XAB; NIST/MONO-177 *Technical Report* (NIST)
[47] Guo X, Zhang K, Liu J, Li Y, Zuo X, Xiao H and He. G 2021 Tensile deformation mechanism of Sn-37Pb solder alloy at cryogenic temperatures *2021 22nd Int. Conf. on Electronic Packaging Technology, ICEPT 2021*
[48] Yan Y, Kim J, Bong U, Jang W, Kim G, Park J and Hahn S 2023 Measurement and analysis of winding stresses in dry-wound pancake coils considering nonlinear compressive behaviors *Supercond. Sci. Technol.* **36** 115019
[49] Molodyk A 2023 Faraday factory: GA-m/year of 2G HTS in prospect synergies for accelerator magnets
[50] Uglietti D 2019 A review of commercial high temperature superconducting materials for large magnets: from wires and tapes to cables and conductors *Supercond. Sci. Technol.* **32** 053001
[51] Van Der Laan D C, Ekin J W, Clickner C C and Stauffer T C 2007 Delamination strength of YBCO coated conductors under transverse tensile stress *Supercond. Sci. Technol.* **20** 765–70
[52] Wang J, Sun C, Cong L, Zhang X and Zhou Y 2019 Delamination strength of HTS tape under transverse tensile stress and its enhancement by using different Ag layer depositing temperatures *Theor. Appl. Mech. Lett.* **9** 147–51
[53] Zhang X, Sun C, Liu C and Zhou Y 2020 A standardized measurement method and data analysis for the delamination strengths of YBCO coated conductors *Supercond. Sci. Technol.* **33** 035005
[54] Senatore C 2024 *Activities of the Wp2.3 at Unige. Focus on Rebco Coated Conductors* (Geneva)
[55] Joshi S, Cozzolino J, Gupta R and Sampson W 2020 Measurements of the effects of compressive loading on the narrow side of the HTS TAPE *IEEE Trans. Appl. Supercond.* **30** 1–5
[56] Du X, Tian Y and Zhao X 2014 Mechanical properties and microstructure of Sn-based solder joints at cryogenic temperature *Proc. Electronic Packaging Technology Conf., EPTC* pp 888–92
[57] Guo X, Xie F, Zuo X, Li Y, Tian R, Liu J and Wang G 2022 Ductile-brittle transition during tensile tests of the general solder alloys at cryogenic temperatures